Electronic Supplementary Material (ESI) for ChemComm.
This journal is © The Royal Society of Chemistry 2018

Supporting Information

Long-range Oriented and Corrugated Structure of the Synthesized Graphene-like Nanosheets

Dongxu He[a], Weidong Xue[a], Zheling Li[b], Alexander J. Marsden[b], Eric Prestat[b,c], Rui Zhao[a*], Wencheng Hu[a], and Mark A. Bissett[b]

[a] Institute of Applied Electrochemistry, School of Materials And Energy, University of Electronic Science and Technology of China, Chengdu 610054, PR China.

[b] School of Materials, National Graphene Institute, University of Manchester, Oxford Road, M13 9PL Manchester, U.K.

[c] SuperSTEM Laboratory, SciTech Daresbury Campus, WA4 4AD Warrington, U.K.

E-mail: ruizhao@uestc.edu.cn

Experimental details

Synthesis procedures

Industrial-grade copper phthalocyanine (β-CuPc, Zibo Fuyan Chemical Industry Co., Ltd.) was used as precursor without further purification. A porcelain boat (12 cm * 6 cm) act as the container. Potassium chloride (KCl) was mixed with CuPc by a household pulverizer. The powders were filled into a porcelain boat and afterwards loaded into an electric furnace equipped with a continuous Argon flow.

The heat treatment was carried out under a nitrogen atmosphere to protect the pyrolysis of CuPc and using the following regime: 1 hour at 30 °C, followed by 4 hours at 500 °C, and finally 8 hours at 800 °C. The ramp rate between each step was 5 °C/min. Then the system was finally cooled to ambient temperature. The product was crushed into a 2L beaker filled with tap water and sonicated for 1 hour. Then, the black sample and salts solution was separated by filtration. Then, they were collected and dried in sequence. The obtained products were denoted by xKCl-GNS, where x refers to the percentage of CuPc in the precursor. Besides, the recrystallized KCl could be reused.

Characterizations

The morphology of the materials were characterized using a scanning electron microscope (SEM, Philips XL30 FEGSEM), transmission electron microscope (TEM, Tecnai G2 20), and atomic force microscope (AFM, JPK Instruments). Samples for AFM characterization were prepared by drop casting of the GNS ethanol solution on a SiO_2/Si wafer. Crystal structure of the samples was investigated by X-ray diffraction (XRD) with a PANalytical X'Pert Pro X'Celerator diffractometer. X-ray photoelectron spectroscopy (XPS) was performed with a Kratos Axis Ultra X-ray photoelectron spectrometer meter; curve fitting was accomplished by CasaXPS software. The optical image was obtained by using a Nikon Eclipse LV100ND microscope. Thermogravimetric analysis (TGA) was carried out under nitrogen atmosphere at a heating rate of 20 °C/min using a TA Q50 series analyser system.

Transmission electron microscopy (TEM), scanning TEM (STEM) imaging and electron diffraction (ED) was further carried out with a FEI Talos F200A. STEM and electron energy loss spectroscopy (EELS) have been performed using a probe side aberration-corrected FEI Titan G2 80–200 kV operating at 200 keV and a Gatan Imaging Filter (GIF) Quantum ER system with a 5 mm entrance aperture (40 mrad collection angle). High-angle annular dark-field (HAADF) imaging were acquired using an inner collection angle of 62 mrad and a probe convergence angle of 21 mrad. Processing the EELS dataset were performed with the open-source HyperSpy library[1] and the Gatan DigitalMicrograph software. Principal component analysis was used to denoise the hyperspectral datasets and 4 to 5 components were used to reconstruct the data. The Cl L, C K, N K and O K maps were obtained by integrating the number of counts in the corresponding edges after background subtraction of the PCA denoised data. The thickness map were measured by the log ratio method[2] and by assuming a inelastic mean path of 151 nm (Iakoubovskii model with a density of 2.266 g/cm3).[3]

The Raman spectra were obtained by using a Raman spectrometer (inVia, Renishaw) equipped with a λ=532 nm laser. The graphene samples are on a SiO_2/Si substrate. The Raman mapping was performed with a step of 0.1 μm for both X axes and Y axes, and ×100 objective was used. For the polarized Raman spectroscopy, the sample was fixed, but the polarization of the incident radiation was rotating, while the scattered radiation was kept polarized in all the directions. The polarization of the laser refers to the polarization of the incident radiation. The angle between the horizontal and the laser polarization direction is defined as θ.

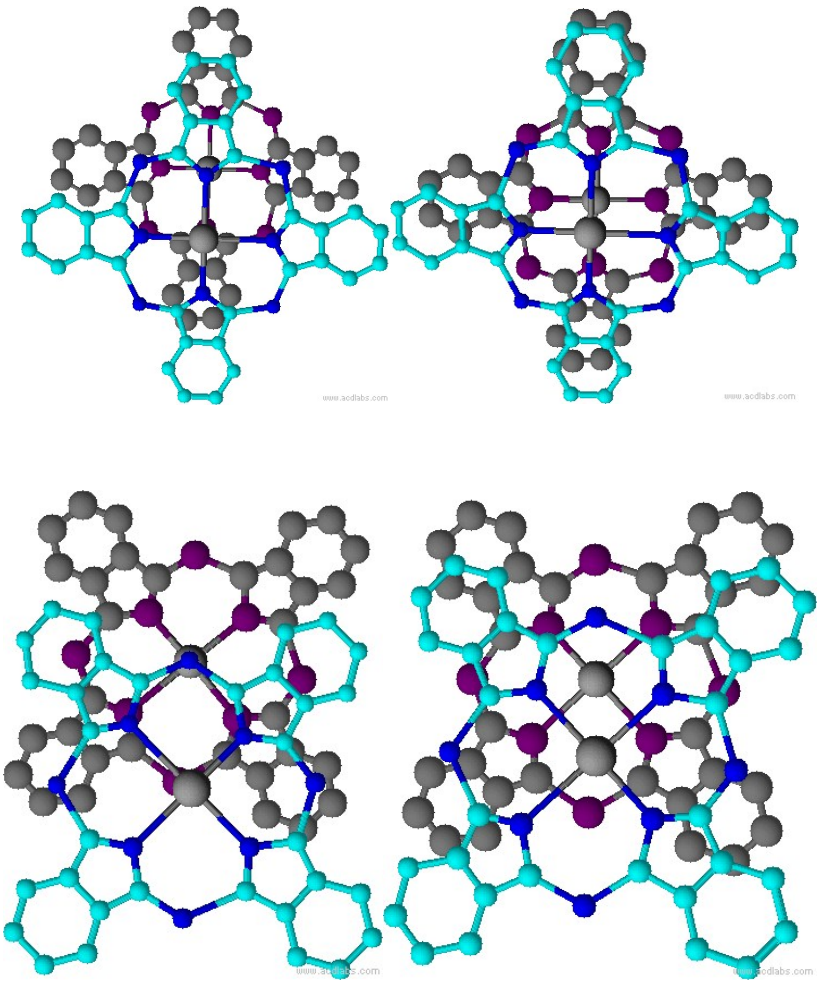

Figure S1. Four different stacking models of CuPc within a molecular column (top view).

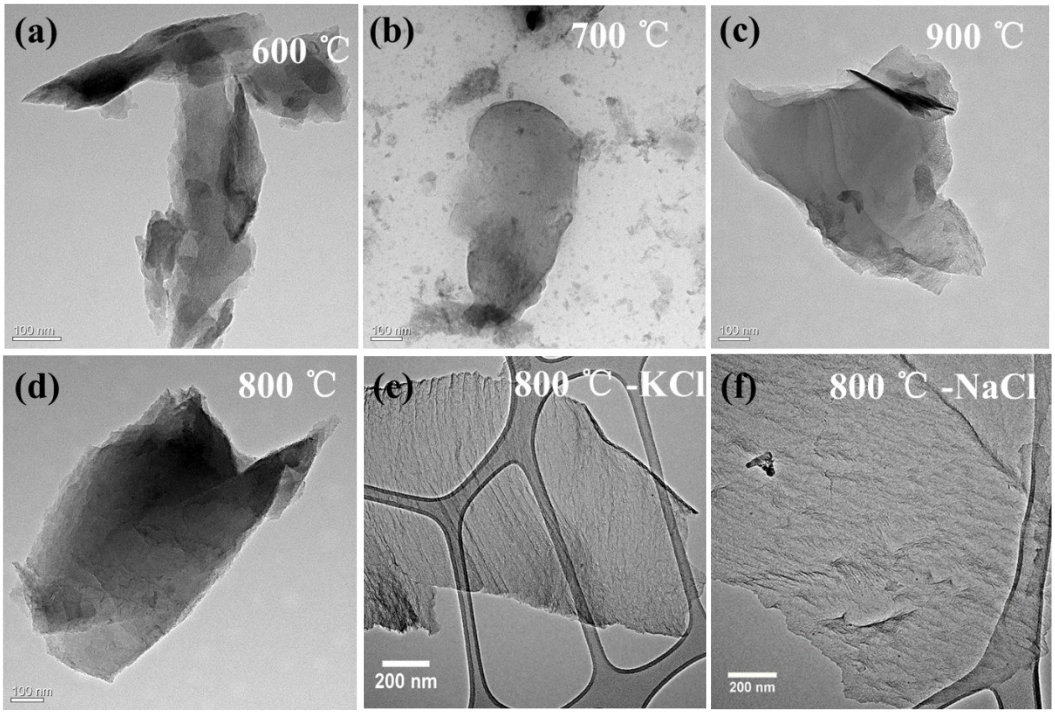

Figure S2 TEM images of the products obtained at temperature of 600 ℃ (a), 700 ℃ (b), 800℃ (d) and 900℃(c); and at 800 ℃ in molten KCl system (e) or molten NaCl system (f).

Intensive studies focused on the morphology effects from different sinter temperature and different pyrolysis media have been fully investigated. The information from thermogravimetric analysis (TGA) of the CuPc (Figure S4) showed the pyrolysis process occurred at ~ 600℃, so the research on the temperature factors has been processed at 600 ℃, 700℃, 800℃ and 900℃, separately.

From the TEM images, Figure S3 (a) and (b), at relative low temperature (600℃ or 700℃), the morphology of the pyrolysis products presented an amorphous structure, and the stacking was obviously. Considering the decomposition temperature of CuPc from TGA curve, incomplete pyrolysis process may be responsible for the last amorphous structure. Only the sintering temperature increased above 800℃, layered structure and the edges of the multilayer flakes can be easily observed, Furthermore, based on our previous work,[1–3] multiple evidences have proved that at the high temperature of 900℃, the heavy graphitization of the products will resulted in the thick graphitic structure in Figure S3(c) .

Pyrolysis media also have been intensively studied, the sintering process with abundant KCl or without KCl at the same temperature gave clearly structured affects. From TEM Figure S3 (d) and (e), the products obtained via the molten KCl system or molten NaCl system were thinner than the ones obtained without molten salt assistance. That was strongly supported our suggestion that the molten salt will act as ‘solvent’ and provide a soft reaction environment. Besides, under the same magnification, only the sample of 1KCl-GNS in Figure S3 (e) shows a regular corrugated surface morphology. It demonstrated that the intermediate precursors formed in the molten salt during the heat treatment played an important role in determining the morphology of the final product. Even though the NaCl has a similar property and closer melting point with KCl, the mismatch between CuPc and NaCl does no help for the assembly of the CuPc but only act as the ‘solvent’. So we can also obtain the thin layer as shown in

Figure S3 (f), and with irregular surface morphology. The same as the products obtained by directly pyrolysis of CuPc (Fiugre S3 (d)). Therefore, it proved that the molten salt system is act as the 'solvent' and promoted the formation of the thin layer, and the kind of the salt influenced the assembly of CuPc and surface morphology.

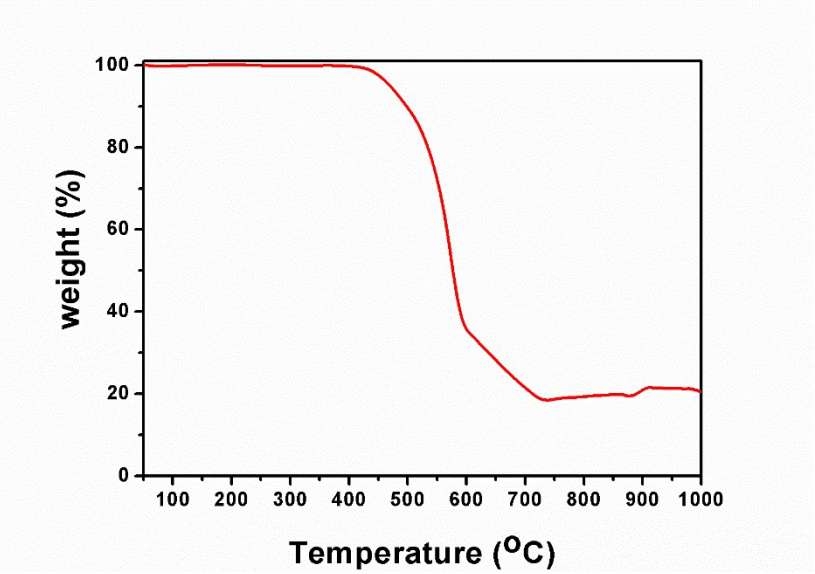

Figure S3 The thermogravimetric analysis (TGA) of the CuPc.

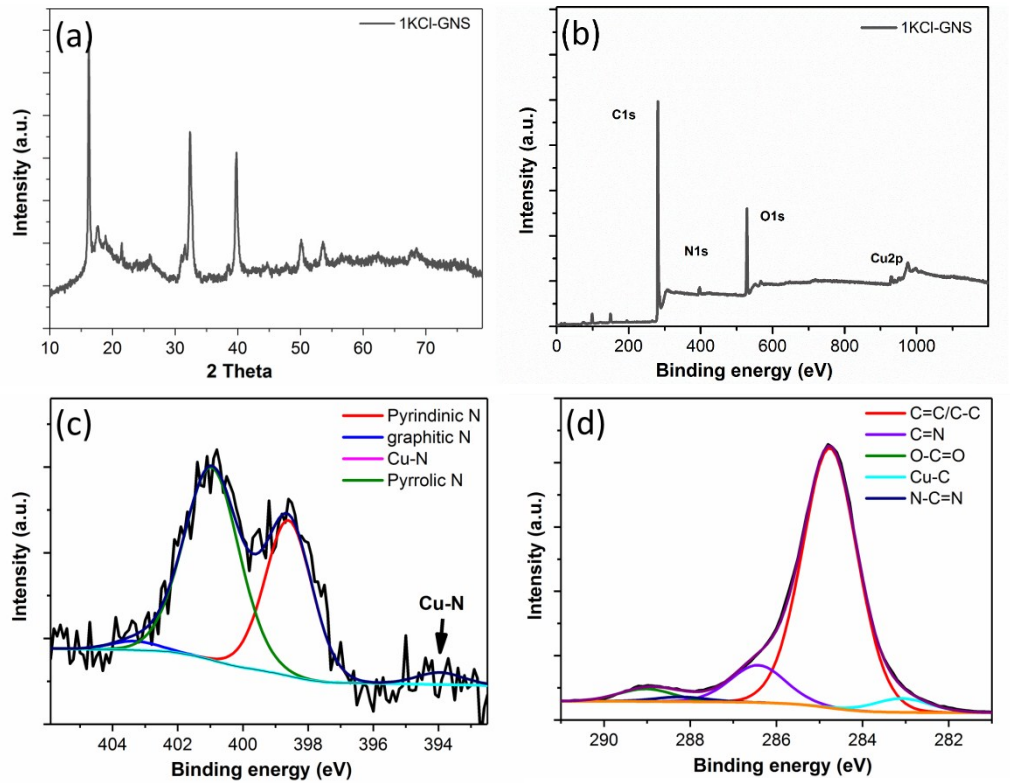

Figure S4. (a) XRD pattern for 1KCl-GNS. (b) Survey X-ray spectroscopic (XPS) characterization for 1KCl-GNS. High resolution XPS spectra for the N 1s (c) and C 1s (e) envelopes of 1KCl-GNS.

XRD and XPS analyzes of the samples were carried out to obtain a better understanding of the synthesized materials composition. The 1KCl-GNS pattern in Figure S2a shows a good correlation with the experimental powder XRD pattern of C_3N_4 (Jade: PDF#50-1250; 15.91, 27.74, 32.14, 39.87, 49.07). Similarly, the peaks around 16.37, 31.94, 39.64, 61.43 and 67.47 are similar with the pattern of $Cu(N_3)_2$ (Jade:PDF#21-0281). The possible structure of the C_3N_4 and $Cu(N_3)_2$,[7,8] implies the preservation of the planar carbon-nitrogen-copper backbone of the CuPc. This indicates that the dehydrogenation and denitrogenation processes occur during the pyrolysis and the organic macromolecules are transformed into an N-doped graphene layer. Additionally, another peak at 26.18˚ is well known as the stacking peak of conjugated aromatic rings, which is comparable to the interplanar stacking distance in crystalline graphite of about 0.34 nm. Considering the dehydrogenation and denitrogenation processes, the nitrogen-linked five or six-membered rings may be the main doping configurations of nitrogen. At high temperature, the strong polarizing nature of the salts offer unparalleled solvation power and facilitates mass transport in a continuous liquid phase, which will effectively restrain the stacking in the third-dimension and result in a relatively lower intensity of the peak around 26˚.

Furthermore, the presence of different bonded nitrogen and carbon atoms can be quantified through analysis of the XPS results. The C 1s, N 1s, O 1s and Cu 2p peaks in Figure S2b appear around 281, 397, 528 and 928 eV, respectively. The N content of 1KCl-GNS was calculated to be 2.0 at. %. Previous related studies have shown that there are four common doping configurations of N in graphene. In Figure S2c, the asymmetric N 1s peak has been divided into four components based on the high resolution scan. The related previous reports have shown that the N 1s binding energy here at 394 eV usually corresponding to the bonding between metal atoms and N.[9–13] Additionally, the XRD analysis (Figure S2a) also supports the

existence of the Cu-N bonding considering the structure of $Cu(N_3)_2$. Therefore, for the sample of 1KCl-GNS, the peak positions at binding energies of 394.0, 398.6, 401.0 and 403.3 eV are attributed to Cu-N bonding, pyridinic N, pyrrolic N and graphitic N respectively.[11,14] XPS results suggest that the predominant bonding configuration of N atoms in 1KCl-GNS is pyridinic N and pyrrolic N. The pyridinic N originated from sp^2 hybridized C atoms at the edges or defects of the graphene lattice. Additionally, evolution of the C 1s XPS peak and fitting components can be seen in Figure S2d. The assignment of the components is based on theoretical predictions of core level shifts and related references.[14–17] The C 1s XPS spectrum of 1KCl-GNS, as shown in Figure S2d, can be deconvoluted into five different peaks centered at 283.1, 284.8, 286.4, 288.2 and 289.0 eV. Typically, the highest intensity peaks centered around 284-285 eV can be assigned to sp^2 and sp^3 hybridized C atoms in graphene.[14,18–20] Peaks at 286.4 eV and 288.2 eV are corresponding to C=N bonding and N=C-N bonding.[21] A low intensity peak at 289.0 eV is attributed to CO type bond.[20] Because the procedure of pyrolysis was under nitrogen atmosphere and without oxygen, the O 1s peak in 1KCl-GNS is possibly due to physisorbed oxygen from atmospheric contamination and adsorbed water. Importantly, considering the previous works about metal-carbon bonding, the peak at 283.08 eV in Figure 3d should be ascribed to C-Cu bonding.[22–25] We suggest that is related to the interaction between the copper atom on one 'face' and the carbon atoms on next 'face' (as shown in Figure S1), thermal treatment results in dehydrogenation but kept the slipped stacking structure and formed the C-Cu bonding.

Table S1. XPS details of the C 1s and N 1s peaks.

KCl-C	Name	Position	Raw Area	Area	fwhm	%At Conc.	Bond Type
	C 1s	284.76	13141.5	76.476	1.7	79.24	C=C/C-C
	C 1s	286.43	1889.97	10.9917	1.7	11.39	C=N
	C 1s	289.03	627.186	3.64414	1.7	3.78	O-C=O
	C 1s	283.08	702.049	4.08807	1.7	4.24	Cu-C
	C 1s	288.22	225.838	1.31257	1.7	1.36	N-C=N
KCl-N	**Name**	**Position**	**Raw Area**	**Area**	**fwhm**	**%At Conc.**	**Bond Type**
	N 1s	398.60	167.328	0.502469	1.9	38.57	Pyrindinic N
	N 1s	403.33	9.70465	0.0291272	1.9	2.24	Graphitic N
	N 1s	393.96	12.964	0.0389485	1.9	2.99	Cu-N
	N 1s	400.96	243.87	0.732128	1.9	56.20	Pyrrolic N

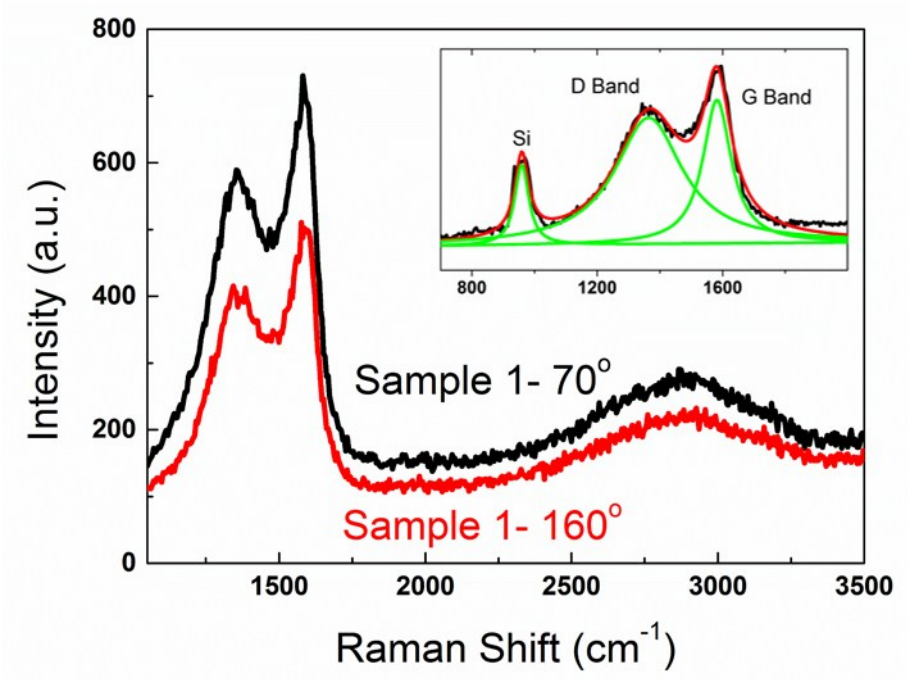

Figure S5. The Raman spectra of one graphene flake of 1KCl-GNS when θ is around 70° (black) and 160° (red), respectively. (Curve fitting is shown as inset.)

The details of the polarized Raman analysis using Eq. 1

For a better understanding of the nanostructure of the layer, we further applied the polarised Raman spectroscopy to identify its intrinsic anisotropic nanostructure. As previously reported,[26] the Raman band intensity stays constant regardless of the angle between the polarisation of the laser and the crystallographic orientation of the sample, for a 'flat' and 'strain-free' graphene flake. However, the Raman band intensity varies as the laser polarisation if the crystallographic structure (e.g. edges)[27] or the spatial orientation[28] of the graphene shows an 'anisotropy', as a result of a change in the Raman polarisability tensor.[29]

The corrugation of graphene studied in this work is one example of the anisotropy. Some graphene samples that have been tested are shown in Figure 4, where 0^o is defined as horizontal direction. The variation of Raman G band intensity (I_G, normalized to the maximum intensity) as the function of angle θ is shown in Figure 4. It can be explained as the corrugation consisting of two distinct parts, where the graphene basal plane can be either perpendicular or parallel to the laser propagation direction. Therefore, the graphene with the basal plane perpendicular to the laser propagation direction shows no laser polarisation dependence[27] while the other one does.[29] Thus the Raman scattering of the graphene corrugation can be a combination of the Raman scattering from the top surface and edge-on of the graphene flake. In order to quantify this anisotropy, similar equation when the Raman band intensity shows a polarisation dependence is used (Eq.1):[27]

$$I_G = A\cos^2(\theta - \theta_o) + B \qquad \textbf{Eq.1}$$

where θ_o is the offset of θ that denotes the angel of the corrugation direction. Since only the incident radiation is polarised, only the square of cosine is used rather than 4^{th} power. Following this equation, the constant of A and B can be obtained by the curve-fitting. It can be seen that I_G gets its maximum when the laser polarisation is parallel to the corrugation direction, and minimum when perpendicular. The values of θ_o are indicated, and it can be seen that all the flakes in Figure 4(a)(c)(e) have different corrugation directions which are difficult to be resolved by the optical micrographs. The I_G variation of the flake in Figure 4(g)(h) does not quite follow the behavior, due to the defective graphene basal plane making a quite irregular corrugation (Figure 4(g)).

In addition to the direction of the corrugation, R, the ratio of $A/(A+B)$ can also be used as a measure of the degree of the corrugation, where the higher the R value, the higher degree of the anisotropy therefore the heavier of the corrugation.[27] This can be understood as, if the graphene is completely flat, then I_G will be constant hence A=0 and B=1. But as the graphene starts to corrugate, the anisotropy increases thus the value of A increases.[27] It can be seen in Figure.4(a)-(c) that all the flakes have R values of over 0.70, demonstrating the anisotropy of the graphene, with the flake in Figure 4(e) having the highest value of R hence the highest degree of corrugation.

Reference

1 S. J. Yoo, C. Y. Kim, J. W. Shin, S. G. Lee, J. M. Jeong, Y. J. Kim, S. H. Lee and J. G. Kim, *Mater. Charact.*, 2013, **78**, 31–36.

2 Pena, F. de la; Tomas, O.; Vidar, T. F.; Pierre, B.; Eric, P.; Petras, J.; Magnus, N.; et al. Hyperspy: v1.4-beta. https://doi.org/10.5281/zenodo.592838.

3 K. Iakoubovskii, K. Mitsuishi, Y. Nakayama and K. Furuya, *Microsc. Res. Tech.*, 2008, **71**, 626–631.

4 D. He, W. Wang, Y. Fu, R. Zhao, W. Xue and W. Hu, *Compos. Part A Appl. Sci. Manuf.*, 2016, **91**, 140–144.

5 W. Xue, H. Xiao, D. He and R. Zhao, *J. Electrochem. Soc.*, 2017, **164**, A2801–A2803.

6 W. D. Xue and R. Zhao, *New J. Chem.*, 2014, **38**, 2993–2998.

7 O. Jana and G. Mani, *New J. Chem.*, 2017, **41**, 9361–9370.

8 M. A. Halcrow, *Chem. Soc. Rev.*, 2013, **42**, 1784–1795.

9 R. Quesada-Cabrera, C. Sotelo-Vazquez, J. A. Darr and I. P. Parkin, *Appl. Catal. B Environ.*, 2014, **160–161**, 582–588.

10 B. Viswanathan and K. R. Krishanmurthy, *Int. J. Photoenergy*, , DOI:10.1155/2012/269654.

11 X. Fei, J. Neilson, Y. Li, V. Lopez, S. J. Garrett, L. Gan, H. J. Gao and L. Gao, *Nano Lett.*, 2017, **17**, 2887–2894.

12 S. Meskinis, M. Andrulevicius, V. Kopustinskas and S. Tamulevicius, *Appl. Surf. Sci.*, 2005, **249**, 295–302.

13 H. Sudrajat, *J. Alloys Compd.*, 2017, **716**, 119–127.

14 H. Wang, T. Maiyalagan and X. Wang, *ACS Catal.*, 2012, **2**, 781–794.

15 J. Li, X. Li, P. Zhao, D. Y. Lei, W. Li, J. Bai, Z. Ren and X. Xu, *Carbon N. Y.*, 2015, **84**, 460–468.

16 Z. Luo, S. Lim, Z. Tian, J. Shang, L. Lai, B. MacDonald, C. Fu, Z. Shen, T. Yu and J. Lin, *J. Mater. Chem.*, 2011, **21**, 8038.

17 F. Joucken, Y. Tison, P. Le Fèvre, A. Tejeda, A. Taleb-Ibrahimi, E. Conrad, V. Repain, C. Chacon, A. Bellec, Y. Girard, S. Rousset, J. Ghijsen, R. Sporken, H. Amara, F. Ducastelle and J. Lagoute, *Sci. Rep.*, 2015, **5**, 1–10.

18 H. Ji, T. Wang, Y. Liu, C. Lu, G. Yang, W. Ding, W. Hou, R. Schlögl and D. S. Su, *Chem. Commun.*, 2016, **52**, 12725–12728.

19 V.-D. Dao, N. T. Q. Hoa, L. L. Larina, J.-K. Lee and H.-S. Choi, *Nanoscale*, 2013, **5**, 12237.

20 C. Zhang, L. Fu, N. Liu, M. Liu, Y. Wang and Z. Liu, *Adv. Mater.*, 2011, **23**, 1020–1024.

21 W.-J. Ong, L.-L. Tan, S.-P. Chai and S.-T. Yong, *Chem. Commun.*, 2015, **51**, 858–861.

22 Q. Zhang, N. Bao, X. Wang, X. Hu, X. Miao, M. Chaker and D. Ma, *Sci. Rep.*, 2016, **6**, 1–15.

23 G. Greczynski, S. Mráz, L. Hultman and J. M. Schneider, *Appl. Surf. Sci.*, 2016, **385**, 356–359.

24 J. Halim, K. M. Cook, M. Naguib, P. Eklund, Y. Gogotsi, J. Rosen and M. W. Barsoum, *Appl. Surf. Sci.*, 2016, **362**, 406–417.

25 Q. Huang, S. Tian, D. Zeng, X. Wang, W. Song, Y. Li, W. Xiao and C. Xie, *ACS Catal.*, 2013, **3**, 1477–1485.

26 G. S. Duesberg, I. Loa, M. Burghard, K. Syassen and S. Roth, *Phys. Rev. Lett.*, 2000, **85**, 5436–5439.

27 P. G. Edges and R. Scattering, 2009, **3**, 45–52.

28 S. Li, Z. Li, T. L. Burnett, T. J. A. Slater, T. Hashimoto and R. J. Young, *J. Mater. Sci.*, 2017, **52**, 9558–9572.

29 Z. Li, R. J. Young, I. A. Kinloch, N. R. Wilson, A. J. Marsden and A. P. A. Raju, *Carbon N. Y.*, 2015, **88**, 215–224.